Advanced Energy Systems and Intelligent Geoscience (AESIG)
https://www.mospbs.com/journal/aesig

• *Article* •

Application of a Geologically Constrained Bayesian Prototypical Network for Few-Shot Lithofacies Identification in Lacustrine Carbonate Rocks

Xiang Cheng[1], Yukun Liu[1,*], Mei Yang[2], Yiming Zhu[1], Yulin Du[1], Xiaolong Wang[1]

[1] Key Laboratory of Exploration Technologies for Oil and Gas Resources (Yangtze University), Ministry of Education, Wuhan 430100, China.

[2] East China University of Technology, Nanchang 330013, China.

***Corresponding Author:** Yukun Liu **Email:** yukunliu@yangtzeu.edu.cn

Received: 10 May 2026 **Accepted:** 12 June 2026

Abstract: Accurate identification of lacustrine carbonate lithofacies is of critical importance for reservoir evaluation. However, conventional deep learning methods face significant bottlenecks in such complex settings, constrained by extreme class imbalance, the absence of uncertainty quantification in deterministic models, and insufficient geological prior knowledge. To address these limitations, this study proposes a Geologically Constrained Bayesian Prototypical Network (GC-BPN) that systematically overcomes these challenges through three synergistic mechanisms. First, the method introduces prototypical network metric learning, which effectively mitigates data scarcity and overfitting tendencies for extreme few-shot classes by learning class prototypes in an embedding space. Second, a Bayesian probabilistic inference framework is constructed to transform deterministic weights into probability distributions, enabling quantitative assessment of predictive uncertainty and providing reliable confidence indicators for lithofacies transition zones. Third, an enhanced Markov transition matrix is constructed by integrating mineral compositional continuity with label transition probabilities, and a Viterbi dynamic programming decoder is employed for global optimal sequence search, significantly suppressing lithofacies discontinuities that violate depositional principles. Systematic validation was conducted using 16,648 labeled samples from five cored wells in the Qianjiang Depression of the Jianghan Basin. Results demonstrate that the GC-BPN achieves an accuracy of 95.47% and a Macro-F1 score of 93.23% on the full-well validation set. The proposed architecture not only achieves breakthroughs in recognizing extreme few-shot classes (e.g., salt rock, granular mixed sedimentary rock) but also exhibits robust performance in blind-well cross-well generalization tests, establishing a new paradigm for intelligent well-log lithofacies identification in complex geological settings.

Keywords: Lacustrine carbonate rock; Lithofacies identification; Bayesian prototypical network; Geological constraint; Uncertainty quantification; Few-shot learning

DOI: https://doi.org/10.58244/aesig.263906

1 Introduction

Lacustrine carbonate rocks constitute a significant class of reservoirs in continental petroliferous basins (Gomes et al., 2020; Zheng et al., 2024). Compared with their marine counterparts, lacustrine systems are governed by multi-source sediment supply, high-frequency paleoclimatic oscillations, and pronounced fluctuations in lake-water salinity. These controls result in more complex mineralogical compositions—characterized by arbitrary mixing proportions of carbonate minerals, terrigenous clastic material, and clay minerals—as well as pronounced depositional heterogeneity, with lithofacies types exhibiting rapid spatial and temporal variations both vertically and laterally (Yang et al., 2016; De Medeiros et al., 2024) . Consequently, the accurate identification of lacustrine carbonate lithofacies is of considerable scientific and engineering significance for reservoir quality assessment, flow unit delineation, and development strategy optimization (Xin et al., 2023).

In recent years, data-driven methods, particularly those employing deep learning, have achieved substantial progress in well-log lithofacies identification. Techniques ranging from classical machine learning algorithms to deep neural network architectures have effectively improved prediction accuracy (Qi and Carr, 2006; Dawson et al., 2023).Nevertheless, in the complex context of lacustrine carbonate rocks, existing methods still encounter three formidable bottlenecks. First, labeled data scarcity and extreme class imbalance (Nawal et al., 2022).Owing to the prohibitively high cost of coring, samples of rare lithofacies are extremely limited—for instance, salt rock accounts for merely 0.7% of the dataset in this study, yielding an imbalance ratio as high as 56.2:1. Under such conditions, purely data-driven models are highly susceptible to overfitting, and transfer learning across lithofacies domains proves largely ineffective (Ding et al., 2024).Second, deterministic models lack uncertainty quantification and are sensitive to label noise (Bao et al., 2023). Within geological transition zones characterized by gradational mineralogical changes, well-log responses exhibit substantial overlap, and conventional networks frequently produce overconfident misclassifications. Concurrently, label noise arising from subjective errors in depth-matching core descriptions to well-log curves severely compromises model training and generalization (Nawal et al., 2022).Third, the absence of geological prior knowledge leads to predictions that violate sedimentary principles (Silva Dos Santos et al., 2025). Most existing models treat individual sampling points as independently and identically distributed, disregarding the vertical gradational pattern dictated by Walther's Law—that is, the first-order Markov property—thereby generating frequent "isolated spikes" or "geologically impossible" discontinuities in predicted profiles (Al-Mudhafar et al., 2025).

To address these limitations, this study proposes a Geologically Constrained Bayesian Prototypical Network (GC-BPN) that systematically overcomes the aforementioned challenges through a tripartite synergistic framework. First, prototypical network metric learning is introduced: by learning class prototypes within an embedding space, few-shot classification is realized, effectively resisting the overfitting tendency induced by scarce labeled data. Second, a Bayesian probabilistic inference framework is constructed, converting deterministic weights into probability distributions. This not only enhances the model's robustness to label noise caused by depth-alignment errors but also, through Monte Carlo sampling, enables quantitative assessment of predictive uncertainty,

yielding reliable confidence metrics for lithofacies transition zones. Third, an enhanced Markov transition matrix is built that fuses mineral compositional continuity information, and a Viterbi dynamic programming decoder is applied to achieve globally optimal lithofacies sequence prediction, markedly suppressing discontinuities that contravene sedimentological principles (Dawson et al., 2023; Aboubacar et al., n.d.) . Taking 16,648 labeled samples from five cored wells in the Jianghan Basin as the study object, this work systematically validates the effectiveness and superiority of the GC-BPN in the automatic identification of complex lacustrine carbonate lithofacies.

2 Geological Background

2.1 Study Area and Lithofacies Classification

The Qianjiang Depression is situated in the central part of the Jianghan Basin (Figure 1.), covering an area of approximately 2,500km², and constitutes a major second-order tectonic unit. Structurally, the Qianjiang Depression displays an overall configuration of two slopes flanking a central sag, forming a double-faulted rhombic depocenter that is elevated in the east and west and depressed in the central region, with the southern portion topographically higher than the northern portion. The study area has experienced two fault-to-sag cycles, developing two sets of source–reservoir successions: the Xingouzui Formation and the Qianjiang Formation. Influenced by intense fault activity and

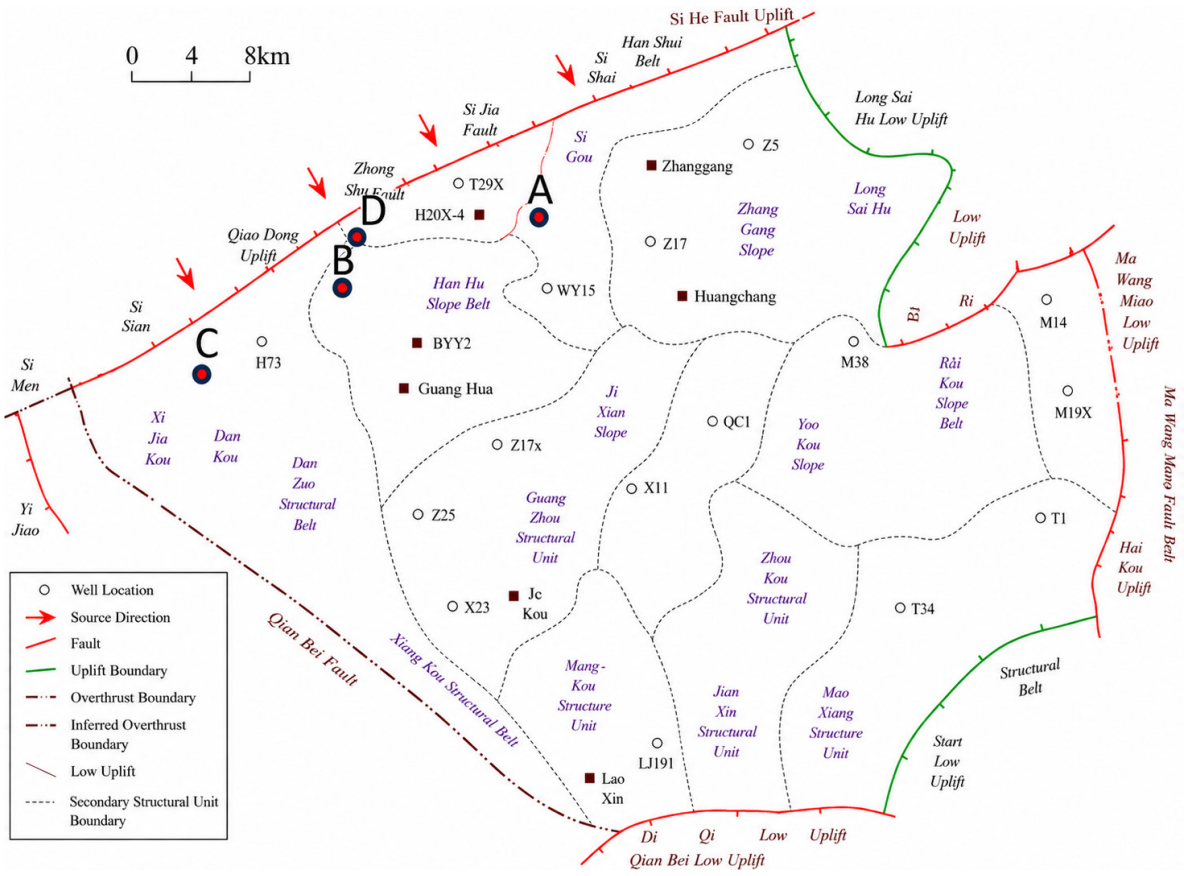

Figure 1. Location of the study area (Qianjiang Depression)

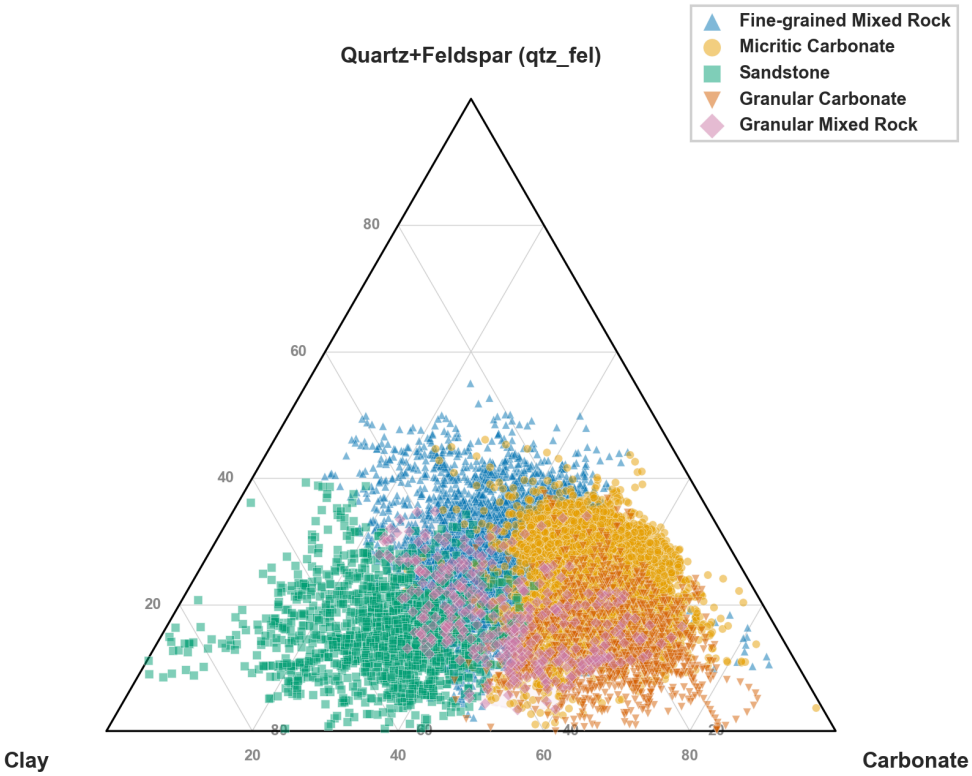

Figure 2. Ternary diagram of mineral composition

rapid subsidence along the Qianbei fault system, the Qianjiang Depression during the deposition of the Qianjiang Formation represented the deepest subsiding and fastest accumulating region within the basin, serving as the primary depocenter. A thick succession of inter-salt oil-bearing strata was deposited, under environmental conditions characterized by high salinity, strong evaporation, restricted circulation, and alternating humid and arid climatic episodes

Based on a three-endmember mineralogical framework (terrigenous clastic / carbonate / clay) in conjunction with sedimentary textural characteristics, the lithofacies of the target interval are classified into six genetic types (Figure 2.): (1) Micritic carbonate, dominated by carbonate minerals with a micritic to microcrystalline texture, reflecting a low-energy, quiet-water depositional environment; (2) Granular carbonate, carbonate-dominated but distinguished by a grain-supported texture, indicative of a high-energy environment; (3) Fine-grained mixed sedimentary rock, in which carbonate and clastic components are juxtaposed in a fine-grained texture, representing the most abundant class in terms of sample count; (4) Granular mixed sedimentary rock, with carbonate grains and clastic material exhibiting mixed support, belonging to an extreme few-shot class; (5) Sandstone, dominated by terrigenous clastic material; and (6) Salt rock, representing chemical precipitates formed under extreme evaporative conditions.

On the mineral-content ternary diagram (Figure 2.), the six lithofacies types display a clear clustering structure: carbonate rocks aggregate near the carbonate endmember, sandstones concentrate near the clastic endmember, and mixed sedimentary rocks distribute across the central

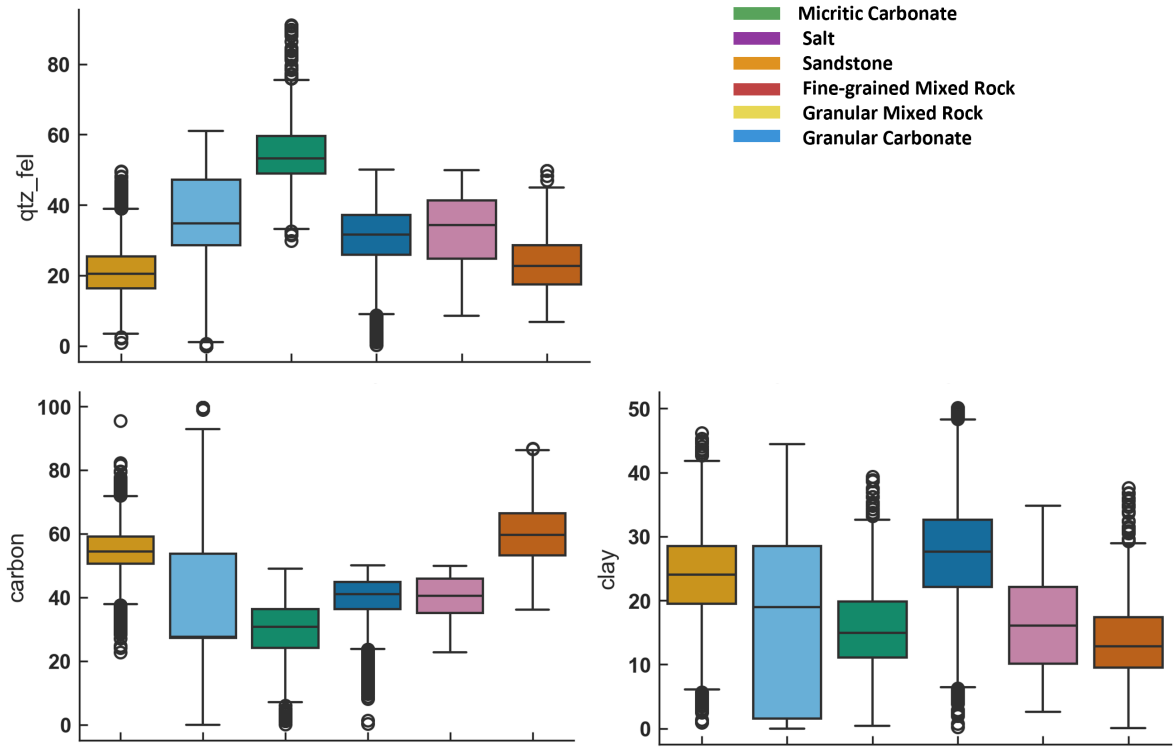

Figure 3. Multi-dimensional box-plot analysis of mineral composition for lacustrine carbonate lithofacies

region, intuitively reflecting the continuous gradational nature between siliciclastic and carbonate lithologies. Box plots (Figure 3.) further quantify the statistical differences among the six lithofacies across the three compositional axes, providing a geological basis for understanding why transitional lithofacies are prone to overlapping well-log responses.

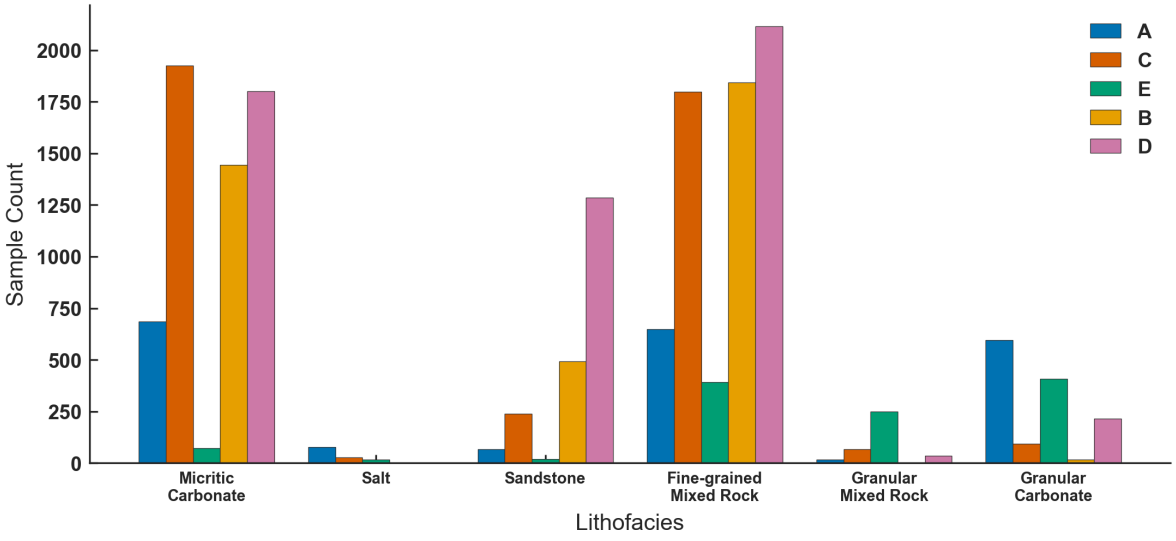

Figure 4. Data distribution across the five cored wells

2.2 Data Sources

In this study, well-log and core description data were acquired from five cored wells (W-A, W-B, W-C, W-D, and W-E). Following depth alignment and quality control, a total of 16,648 labeled samples were obtained. The spatial distribution of the five wells effectively covers the principal sedimentary facies belts of the study area, with

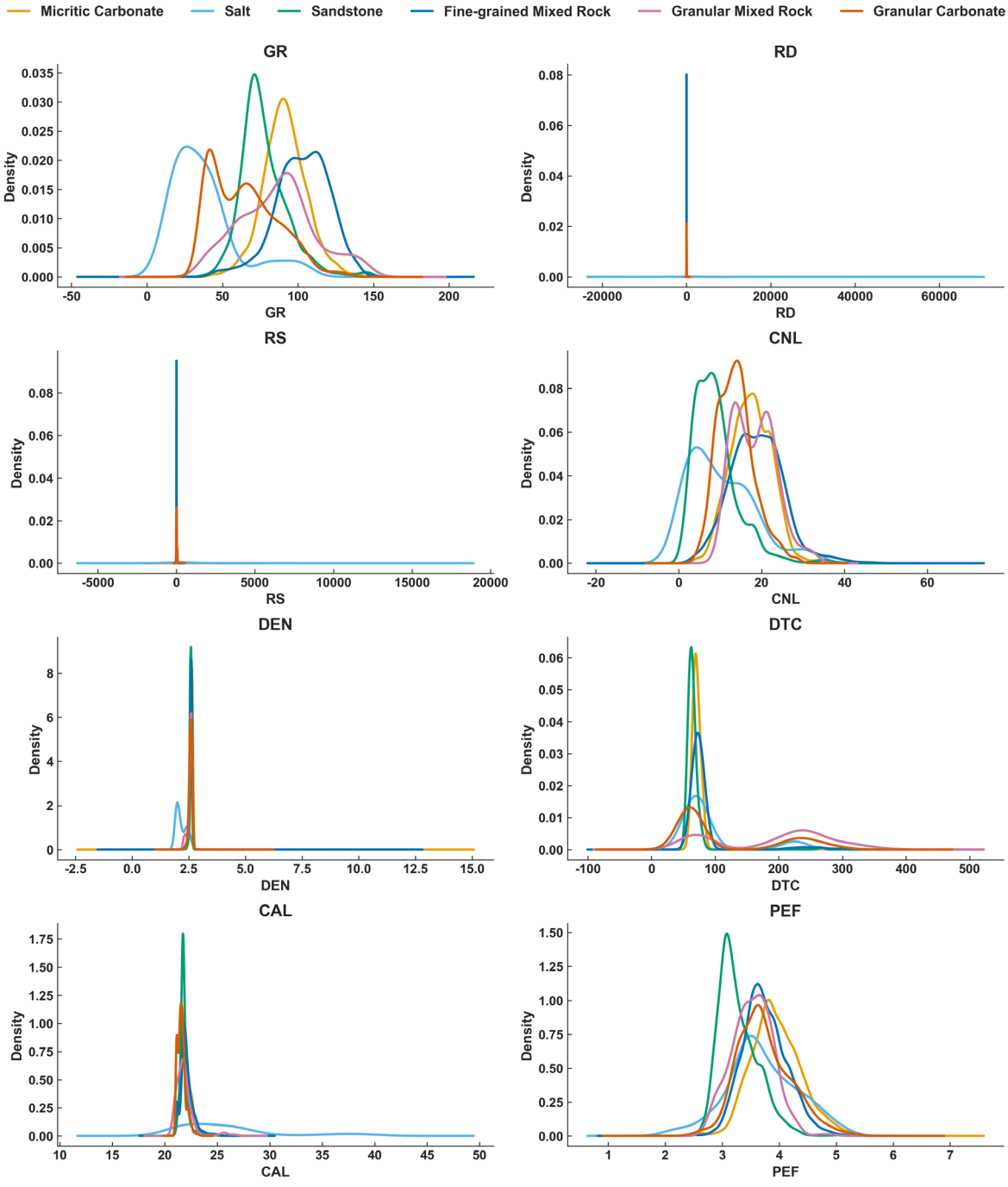

Figure 5. Distribution of well-log response characteristics for the six lithofacies types (after normalization)

Wells W-D and W-C yielding the largest datasets (5,450 and 4,150 samples, respectively) and Well W-E providing the smallest dataset (1,158 samples) (Figure 4.). The original well-log suite comprised eight curve types. The compensated neutron log (CNL) was excluded from Well W-E owing to extensive data gaps; ultimately, seven well-log types—GR, RD, RS, DEN, DTC, CAL, and PEF—were retained as primary input features to ensure inter-well consistency and physical reliability of input variables. The dataset exhibits severe class imbalance, with the ratio of the most abundant to the least abundant class reaching 56.2:1. This pronounced "long-tail distribution" further underscores the challenges associated with applying conventional data-driven methods(Mohammadi et al., 2025) . The response characteristics of each lithofacies type across different well-log curves are illustrated in Figure 5.. Micritic carbonate and granular carbonate show marked differences in bulk density (DEN) and photoelectric absorption index (PEF), whereas the mixed sedimentary rock classes display substantial response overlap across all log curves, which physically explains the inherent difficulty in classifying transitional lithofacies.

3 Methodology

3.1 Prototypical Network (ProtoNet)

The prototypical network is a few-shot classification method grounded in metric learning. Its core principle is as follows: an encoder maps input samples into a low-dimensional embedding space; class prototypes are computed as the mean of the embedded support set samples for each class; and query samples are classified according to their Euclidean distance to each class prototype. Given an encoder f_ϕ, the prototype of class k is defined as the mean embedding of c_k samples belonging to that class's support set:

$$c_k = \frac{1}{|S_k|} \sum_{x_i \in S_k} f_\phi(x_i) \tag{1}$$

where S_k denotes the support set of class k, $|S_k|$ is the number of samples in that set, x_i denotes the i-th sample in the support set, $f_\phi()$ represents the feature embedding network, and ϕ denotes the network parameters.

Once the prototype of each class is obtained, the probability that a query sample x belongs to class k is computed via a softmax function:

$$p(y = k \mid x) = \frac{\exp\left(-\| f_\phi(x) - c_k \|^2\right)}{\sum_{k'} \exp\left(-\| f_\phi(x) - c_{k'} \|^2\right)} \tag{2}$$

where $f_\phi(x)$ denotes the embedding representation of the query sample x, c_k is the prototype of class k, $\| f_\phi(x) - c_k \|^2$ represents the squared Euclidean distance between the query sample and the class prototype, and the denominator sums over all classes k' to achieve probability normalization. This formulation converts distances into a probability distribution by computing the relative distance from the query sample to each class prototype, ultimately assigning the sample to the class with the highest probability.

In this study, the ProtoNet encoder adopts a three-layer MLP architecture, with each layer comprising a fully connected layer, batch normalization, and a ReLU activation function. The input dimensionality is 17, encompassing seven original well-log features, seven derived features, and three mineral-composition auxiliary features. Training employs an episodic training strategy: each episode is randomly sampled, and the loss function is a class-weighted cross-entropy loss, with weights inversely proportional to the sample count of each class.

3.2 Bayesian Prototypical Network (BPN)

The BPN replaces the deterministic encoder with a hybrid Bayesian encoder, achieving uncertainty quantification through probabilistic weight distributions (Bao et al., 2023)reservoir prediction plays a significant role since it can reveal the characteristics of a reservoir through attribute analysis. Multi-attribute reservoir prediction models are the most commonly used methods that aim to establish a reasonable relationship between reservoir parameters and seismic attributes. Although many related approaches have been proposed, their results are unsatisfactory when given limited logging data. Meanwhile, they frequently fail to evaluate how reliable their predictions are. Given the prominent advantages of Bayesian methods to model uncertainty, we propose in this paper a Bayesian neural network (BNN . The core component is the Bayesian linear layer, in which weights W false and biases b are no longer fid values but instead follow Gaussian distributions with learnable parameters:

$$W \sim \mathcal{N}\left(\mu_W, \sigma_W^2\right), \sigma_W = \log\left(1+\exp\left(\rho_W\right)\right) \quad (3)$$

where μ_W denotes the mean parameter of the weights, σ_W denotes the standard deviation of the weights, and ρ_W is the learnable log-standard-deviation parameter, with a softplus function $\log\left(1+\exp\left(\rho_W\right)\right)$ applied to ensure positivity of the standard deviation. During training, the network learns the parameters μ_W and ρ_W, while the weights W are sampled from this distribution via the reparameterization trick.

During training, a set of weights is drawn from this distribution via the reparameterization trick; during inference, the distribution of predicted probabilities is obtained through multiple Monte Carlo (MC) forward passes. The Bayesian prior constraint is implemented through KL divergence regularization:

$$\mathrm{KL}\left[\mathcal{N}\left(\mu,\sigma^2\right) \| \mathcal{N}\left(0,1\right)\right] = \frac{1}{2}\Sigma\left(\sigma^2+\mu^2-2\log\sigma-1\right) \quad (4)$$

where $\mathrm{N}\left(\mu,\sigma^2\right)$ denotes the learned posterior distribution, $\mathrm{N}(0,1)$ denotes the standard normal prior distribution, and μ and σ are the mean and standard deviation of the posterior distribution, respectively. This formulation regularizes the model and prevents overfitting by minimizing the KL divergence between the posterior and prior distributions.

During the inference stage, the mean predicted probability is obtained through T MC forward passes, from which two uncertainty metrics are derived: (1) predictive entropy (total uncertainty), which reflects the overall degree of uncertainty in the model's individual predictions; and (2) mutual information (epistemic uncertainty), which can accurately capture knowledge blind spots arising from insufficient training data. These metrics provide critical confidence indicators for practical oilfield applications, enabling engineers to explicitly identify and exercise caution with predictions for which the model may be "overconfident."

3.3 Complete GC-BPN Architecture

The GC-BPN model, which introduces two tiers of geological constraints on top of the BPN framework (overall architecture shown in Figure 6.), fully exploits the pronounced Markov property inherent in stratigraphic depositional sequences—namely, that the probability of adjacent depth intervals belonging to the same lithofacies is substantially higher than the probability of an abrupt change (Abdel-Fattah et al., 2022)the Upper Cretaceous Khasib Formation is the largest producing carbonate reservoir. The basic architecture of the "Khasib reservoirs" is heavily impacted by the lithofacies classification and sequence

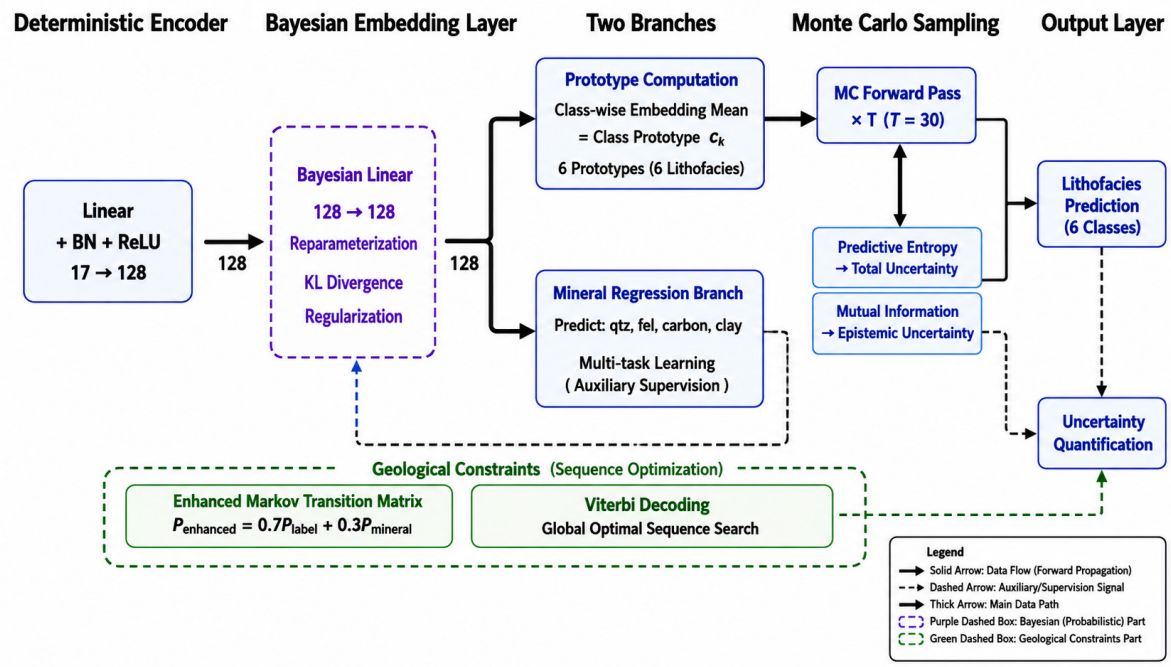

Figure 6. Architecture of the GC-BPN model

stratigraphic interpretation at East Baghdad field. A description of the Khasib Formation in terms of depositional systems, environments and lithofacies was obtained by studying the vertical distribution of the lithofacies, defined using well-log values and their mutual statistical relationships and constrained by the core data (thin sections . The model integrates two types of geological prior information from the training data to construct this enhanced transition matrix. Specifically, a label transition probability matrix P_label is derived by counting the frequency of lithofacies transitions between adjacent sampling points and applying normalization:

$$A_{ij}^{label} = \frac{\text{Count}(y_t = i, y_{t+1} = j)}{\sum_{j'} \text{Count}\left(y_t = i, y_{t+1} = j'\right)} \quad (5)$$

where y_t denotes the label at time step t, $\text{Count}(y_t = i, y_{t+1} = j)$ counts the occurrences in the training set where label i is immediately followed by label j, and the denominator sums over all possible subsequent labels j' for normalization. This matrix captures the transition patterns of label sequences and can be employed to constrain the model's predictions.

Concurrently, a mineral continuity matrix P_mineral is obtained by computing the cosine similarity between mineral composition vectors of adjacent sampling points and normalizing:

$$A_{ij}^{mineral} = \frac{\sum_{t:y_t=i,y_{t+1}=j} \cos\left(m_t, m_{t+1}\right)}{\sum_{j'} \sum_{t:y_t=i,y_{t+1}=j'} \cos\left(m_t, m_{t+1}\right)} \quad (6)$$

where m_t denotes the feature vector at time step t, and $\cos\left(m_t, m_{t+1}\right)$ computes the cosine similarity between feature vectors of adjacent time steps. This formulation employs weighted similarity rather than simple counting, enabling a more nuanced characterization of the transition relationships among mineral components. The resulting fused matrix (Figure 7) not only reflects the vertical gradational pattern of strata through its diagonal dominance, but its off-diagonal elements also accurately capture the transition probabilities at lithofacies boundaries.

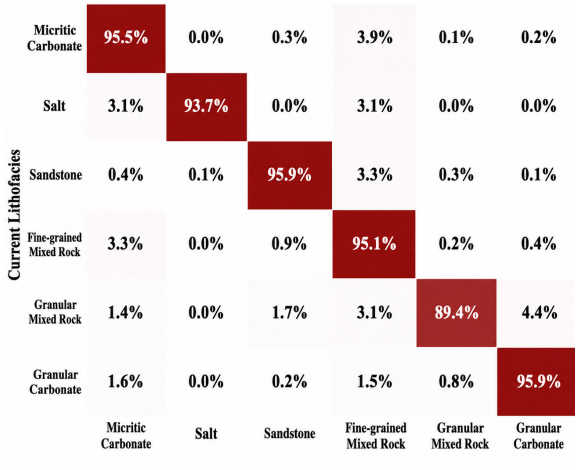

Figure 7. Enhanced Markov transition matrix

3.4 Feature Engineering and Data Partitioning

Building upon the seven original well-log curves, seven derived features were computed in this study (Table 1): logarithm of deep resistivity log10(RD), logarithm of shallow resistivity log10(RS), resistivity ratio RD/RS, lithology–density ratio GR/DEN, photoelectric–gamma product PEF×GR, density–photoelectric difference DEN−PEF, and acoustic impedance DEN×DTC. The resulting 14 well-log features were standardized using Z-score normalization. To rigorously prevent information leakage, the StandardScaler was fitted exclusively on the training set and subsequently applied to the validation and test sets.

This study adopts a two-stage data partitioning strategy to comprehensively evaluate model performance. Stage A (global mixed evaluation): samples from all five wells are pooled and randomly split in an 80/20 ratio stratified by the target variable, with the objective of establishing the model's benchmark performance ceiling within the known geological distribution. Stage B (blind-well cross-well evaluation): Well W-B is designated as a fully independent blind well (100% of its samples constitute the test set), while the remaining four wells are split in an 80/20 ratio following a strictly depth-continuous sequence. This depth-sequential partitioning strategy effectively mitigates the risk of data leakage arising from spatial autocorrelation in well-log data, and its objective is to rigorously test the model's cross-well generalization capability when confronted with unseen well intervals.

Table 1. Derived features

Derived Feature	Formula	Physical Interpretation
Logarithm of deep resistivity	log10(RD)	Compaction-corrected resistivity, compresses order-of-magnitude differences
Logarithm of shallow resistivity	log10(RS)	Compaction-corrected shallow resistivity
Resistivity ratio	RD/RS	Resistivity contrast between invaded zone and undisturbed formation; fluid property indicator
Lithology–density ratio	GR/DEN	Ratio of natural radioactivity to bulk density; lithology-sensitive
Photoelectric–gamma product	PEF×GR	Composite lithology indicator integrating photoelectric absorption and radioactivity
Density–photoelectric difference	DEN−PEF	Difference between density and photoelectric index; composite lithology–petrophysical indicator
Acoustic impedance	DEN/DTC	Wave impedance; composite lithology–petrophysical parameter

4 Results and Discussion

4.1 Progressive Performance Comparison of the Three Models

Under the Stage A global mixed validation, the baseline fitting capacity of each model within the known geological distribution was thoroughly evaluated (Table 2). As the baseline, the ProtoNet model yielded satisfactory identification performance for the majority classes with adequate sample representation; however, constrained by class imbalance, it exhibited severe inter-class confusion for the minority class of granular mixed sedimentary rock (Figure 8.). The introduction of the BPN model partially alleviated this issue, substantially improving overall identification accuracy. Nevertheless, its comparatively high expected calibration error revealed a tendency toward overconfidence in probabilistic outputs.

By contrast, the proposed GC-BPN model achieved an optimal balance between classification performance and predictive reliability through the incorporation of geological constraints, attaining an accuracy of 95.47% and a Macro-F1 score of 93.23%. Furthermore, the training dynamics (Figure 9.) confirmed that the model converged rapidly without exhibiting discernible overfitting, demonstrating excellent generalization stability and computational efficiency. These characteristics also laid a solid foundation for the subsequent cross-well generalization tests in Stage B.

Table 2. Performance comparison of the three models on the full-well validation set

Model	Accuracy	Macro -F1	Weighted -F1	Optimal Epoch
ProtoNet	0.7787	0.7145	0.7872	48
BPN	0.8562	0.8260	0.8574	99
GC-BPN	0.9547	0.9323	0.9547	143

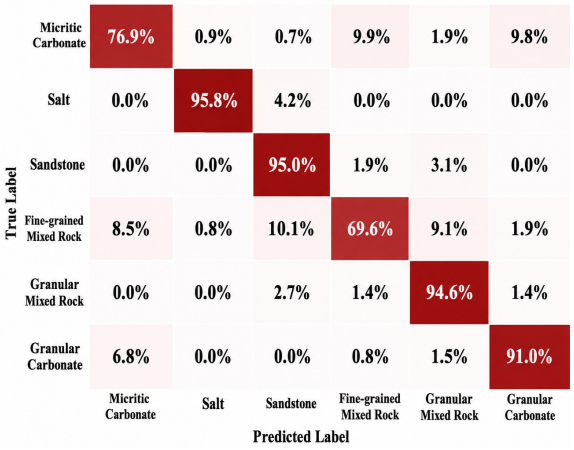

Figure 8. Confusion matrix of ProtoNet

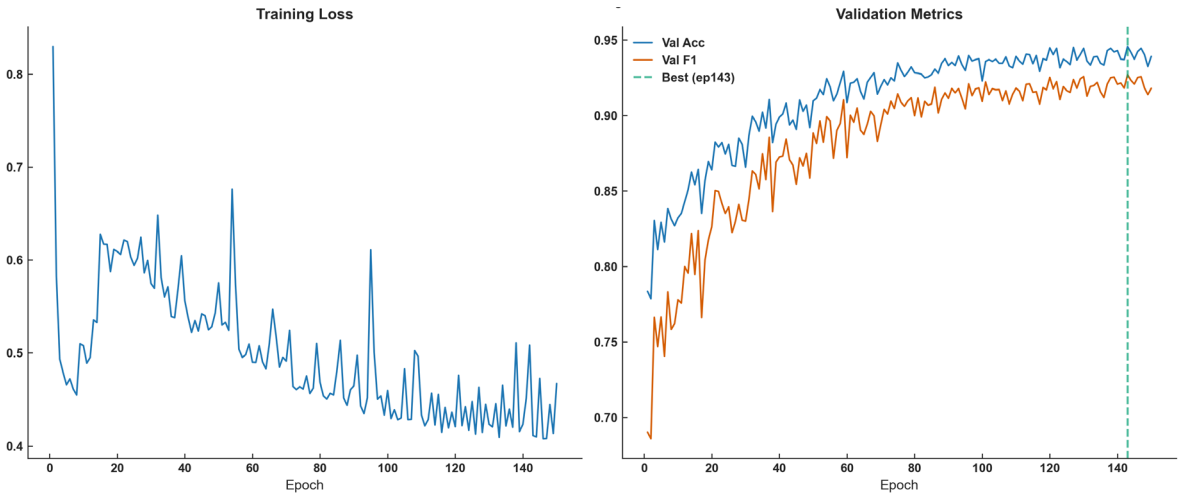

Figure 9. Training process curves of the GC-BPN model

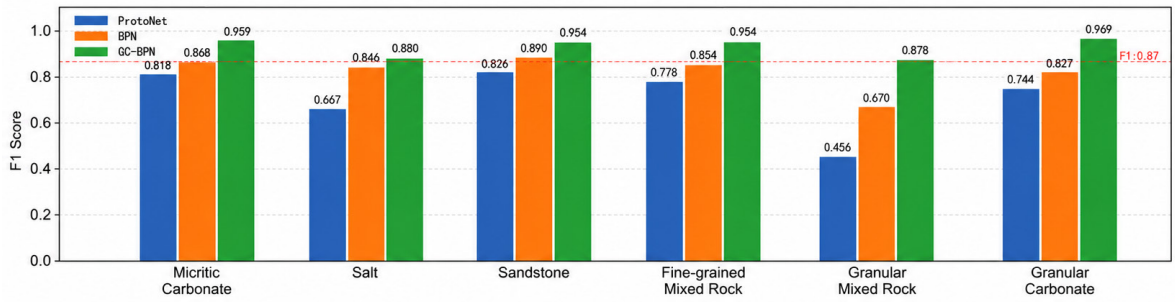

Figure 1.0 Per-class F1-score comparison

As illustrated in Figure 1.0, the GC-BPN maintains F1 scores above 0.87 across all six lithofacies types, demonstrating a clear performance advantage. The model achieves exceptionally high identification rates (F1 > 0.95) for well-represented conventional lithofacies such as sandstone and carbonate rocks. More importantly, for extreme few-shot classes such as salt rock and granular mixed sedimentary rock, the F1 scores nonetheless reach approximately 0.88. Compared with the baseline models, the GC-BPN yields a near-doubling of the F1 score for granular mixed sedimentary rock, convincingly demonstrating the critical role played by Bayesian inference and geological prior constraints in overcoming class imbalance and enhancing the recognition of minority classes.

The incorporation of Viterbi post-processing further corrected 52 isolated prediction discontinuities, raising the model's accuracy and Macro-F1 to 95.47% and 93.23%, respectively, and effectively ensuring the vertical continuity of geological sequences. The confusion matrix (Figure 1.1) shows that the predictions of the GC-BPN are highly concentrated along the diagonal, with extremely low misclassification rates for all classes. The t-SNE feature visualization (Figure 1.2) further indicates that the six lithofacies types form well-defined and compact cluster boundaries in feature space, exhibiting excellent inter-class separability.

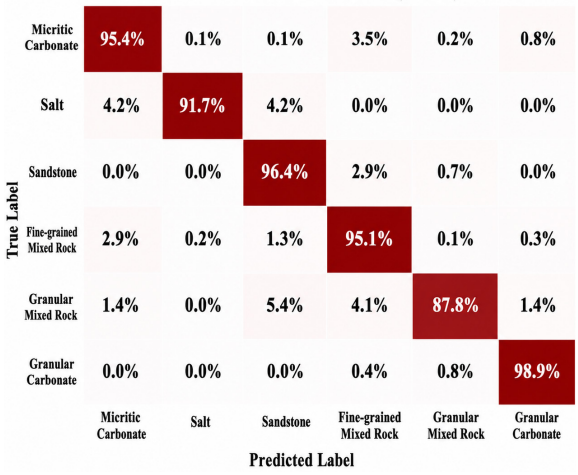

Figure 1.1 Confusion matrix of GC-BPN

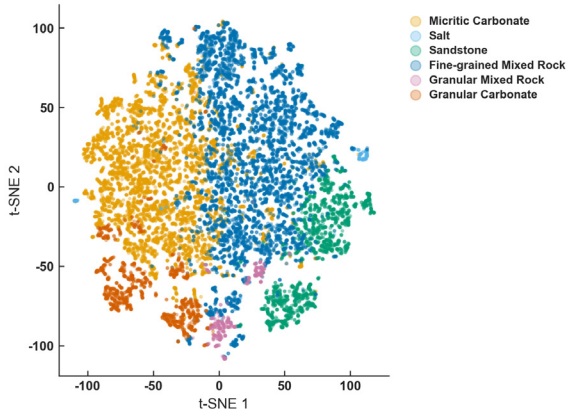

Figure 1.2 t-SNE embedding visualization of GC-BPN

4.2 Uncertainty Analysis

To further investigate the reliability of the model's predictions and the underlying physical significance, a quantitative decomposition analysis of prediction uncertainty was conducted. The results

demonstrate that, following the introduction of geological constraints, the mean predictive entropy of the GC-BPN was markedly reduced to 0.13, indicating a substantial improvement in the model's prediction confidence. Within the uncertainty budget of the GC-BPN, epistemic uncertainty accounts for merely ~5.7% of the total predictive entropy. This suggests that the model has adequately captured the discriminative boundaries of all classes, and that the residual total uncertainty is predominantly governed by the intrinsic aleatoric uncertainty of the data. By contrast, although the BPN model's uncertainty is similarly dominated by aleatoric uncertainty, its expected calibration error reaches as high as 0.0784, exposing a pronounced overconfidence bias: within intermediate confidence intervals, the actual accuracy is notably lower than the predicted confidence. This phenomenon represents a canonical deficiency of purely data-driven models in the absence of spatial geological constraints, thereby underscoring the necessity of incorporating geological prior constraints to calibrate probabilistic outputs (Bao et al., 2023reservoir prediction plays a significant role since it can reveal the characteristics of a reservoir through attribute analysis. Multi-attribute reservoir prediction models are the most commonly used methods that aim to establish a reasonable relationship between reservoir parameters and seismic attributes. Although many related approaches have been proposed, their results are unsatisfactory when given limited logging data. Meanwhile, they frequently fail to evaluate how reliable their predictions are. Given the prominent advantages of Bayesian methods to model uncertainty, we propose in this paper a Bayesian neural network (BNN; Mohammadian et al., 2022).

Both Pearson and Spearman correlation analyses indicate that samples with high predictive entropy are strongly concentrated within mineral compositional transition zones. From the perspective of well-log response mechanisms, gradational changes in mineral composition—for example, the evolution from fine-grained mixed sedimentary rock to micritic carbonate—cause the well-log response characteristics of different lithofacies to overlap spatially, forming ambiguous decision boundaries.

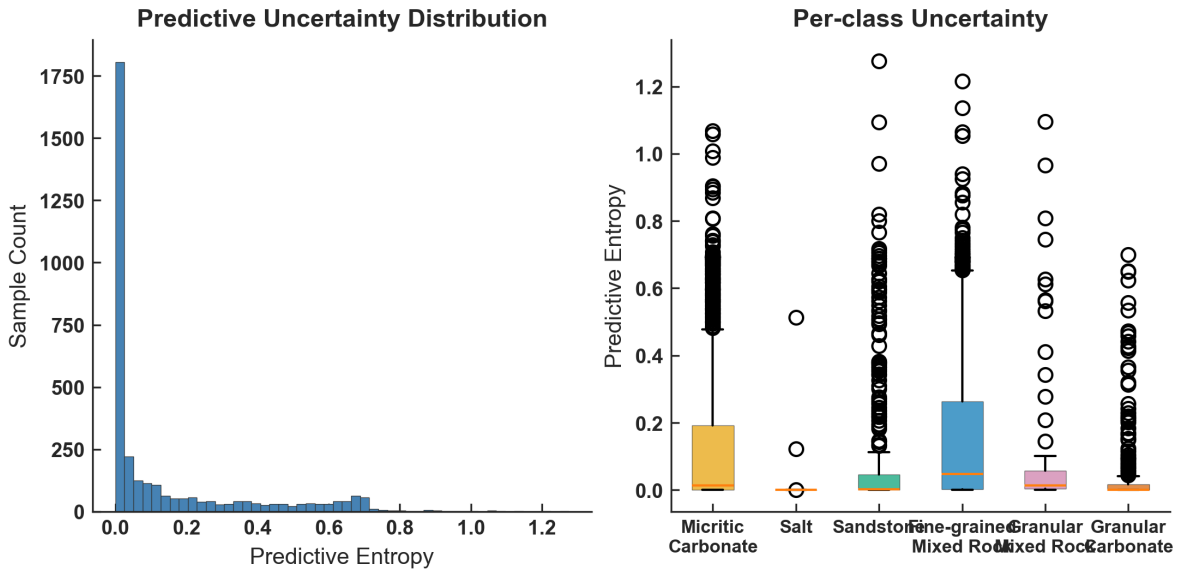

Figure 1.3 Uncertainty analysis of GC-BPN

This uncertainty, arising from the intrinsic ambiguity of the data, fundamentally reflects the inherent overlap of well-log responses (aleatoric uncertainty) together with the model's limited discriminative capacity for samples located in transition zones (epistemic uncertainty). The t-SNE feature space visualization, color-coded by mineral composition, provides further intuitive confirmation of this pattern: a distinct gradational transition zone forms between samples with high carbonate content and those with high clay content, and the predictive entropy of samples within this transition zone reaches peak values (Figure 1.3). This convincingly demonstrates that predictive entropy can serve as an effective indicator for quantifying the ambiguity of geological transition zones.

4.3 Blind-Well Generalization Experiment

Having validated the model's excellent fitting capacity within the known geological distribution, it is essential to further assess its cross-well generalization capability when confronted with unseen well intervals. To this end, Stage B was designed as a semi-blind test with Well W-B designated as the target blind well (Table 3). The results show that the GC-BPN maintains its performance lead, achieving an accuracy of 76.01% and a Macro-F1 of 69.74%, significantly outperforming both ProtoNet and BPN.

In terms of absolute metrics, the GC-BPN's performance on the blind well surpasses that of BPN and ProtoNet by 7.40 and 6.20 percentage points, respectively, convincingly demonstrating that its learned geological representations possess superior cross-well transfer potential. At the class level, the GC-BPN retains relatively strong identification capability for salt rock and micritic carbonate, with F1 scores reaching 0.889 and 0.786, respectively; however, the recognition rate for granular mixed sedimentary rock declines sharply, with an F1 of only 0.237. This indicates that, under cross-well generalization scenarios, the accurate identification of extreme few-shot classes remains a formidable challenge yet to be resolved.

4.4 Ablation Experiment

To quantify the individual contribution of each key component, an incremental ablation experiment was designed (Figure 1.4). The results indicate that the probabilistic inference module (Bayesian layers and MC sampling) makes the most substantial contribution: it not only effectively alleviates overfitting through regularization—yielding a Macro-F1 improvement of 0.0132—but also furnishes the model with a theoretical framework for uncertainty quantification. Concurrently, the geological Markov constraint introduced via Viterbi post-processing effectively suppresses isolated prediction discontinuities in the well-log sequence. It is noteworthy that, although class weighting yields only a marginal direct gain under the high autocorrelation conditions of same-well training, it proves critical in cross-well generalization: it effectively prevents the features of minority classes from being overwhelmed by majority classes under domain shift, enabling the

Table 3. Performance comparison of the three models on blind Well B

Model	Accuracy	Macro-F1	Weighted-F1	Generalization Gap (Acc)
ProtoNet	0.6981	0.5887	0.7275	8.06 pp
BPN	0.6861	0.5809	0.7097	17.01 pp
GC-BPN	0.7601	0.6974	0.7764	19.46 pp

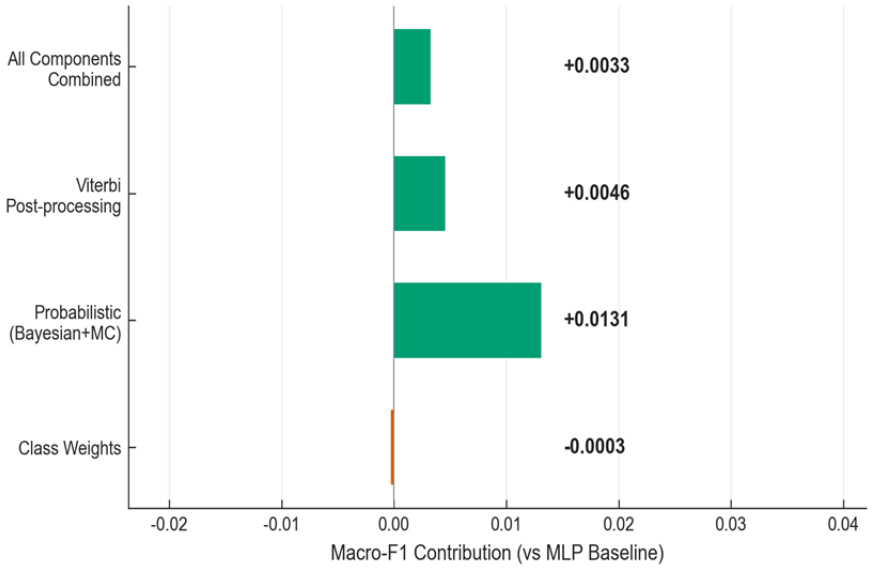

Figure 1.4 Independent contribution of each component to Macro-F1 in the ablation experiment

GC-BPN to achieve a substantial performance lead with an accuracy of 76.01% in the Stage B blind-well test. Ultimately, the fully integrated GC-BPN, with all components operating synergistically, attains the optimal comprehensive performance, with accuracy and Macro-F1 reaching 0.9547 and 0.9323, respectively.

5 Conclusions

To overcome the three principal bottlenecks encountered in lacustrine carbonate lithofacies identification—namely, labeled data scarcity, the absence of uncertainty quantification, and insufficient integration of geological prior knowledge—this study proposes a Geologically Constrained Bayesian Prototypical Network (GC-BPN). Based on the tripartite synergistic mechanisms of this model, the following main conclusions are drawn:

Under full-well validation, the GC-BPN demonstrates excellent comprehensive performance, significantly surpassing existing baseline models. Notably, the model effectively mitigates the data class imbalance problem, substantially improving the identification accuracy of extreme few-shot classes such as salt rock and granular mixed sedimentary rock. This finding robustly validates the effectiveness of Bayesian inference and class-weighting strategies in feature representation learning.

By constructing an enhanced Markov matrix that fuses label transition probabilities with mineral continuity information, and by coupling this with the Viterbi global decoding algorithm, the model effectively suppresses isolated lithofacies discontinuities that violate sedimentological principles, thereby markedly enhancing the geological plausibility and vertical continuity of the interpreted well-log profiles. Furthermore, the introduction of geological constraints significantly calibrates the model's prediction confidence, substantially reducing predictive entropy. The study reveals a significant positive correlation between predictive entropy and mineral compositional ambiguity. This not only elucidates the intrinsic mechanism underlying overlapping well-log responses in transition zones but also provides a novel analytical tool for the quantitative characterization of geologically ambiguous boundaries.

Under rigorous semi-blind well testing, the core

metrics of the GC-BPN remain significantly ahead of those of the comparative models, demonstrating excellent cross-well generalization potential. In view of current limitations, future work will focus on three directions: first, exploring approximate mineral content estimation methods based on well-log curve morphological features to reduce the model's dependence on measured mineralogical data; second, incorporating higher-order Markov chains or Hidden Markov Models (HMM) to more accurately capture complex vertical depositional cyclicity; and third, deeply integrating domain adaptation and active learning strategies to further overcome the cross-well generalization bottleneck of the model.

Acknowledgments

The authors would like to thank all individuals and institutions that contributed to this study.

Funding Statement

This work was supported by the Open Fund of the SINOPEC Key Laboratory of Geophysics (Grant No. 36750000-24-FW0399-0002) and the Natural Science Foundation of Hubei Province, China (Grant No. 2024AFB271).

Author Contributions

All authors contributed to the study conception and design, data collection, analysis and interpretation of the results, and manuscript preparation, and take responsibility for the integrity of the work.

Availability of Data and Materials

None.

Conflicts of Interest

The authors declare that they have no conflicts of interest to report regarding the present study.

References

[1] Abdel-Fattah, M. I., Mahdi, A. Q., Theyab, M. A., Pigott, J. D., Abd-Allah, Z. M., & Radwan, A. E. (2022). Lithofacies classification and sequence stratigraphic description as a guide for the prediction and distribution of carbonate reservoir quality: A case study of the Upper Cretaceous Khasib Formation (East Baghdad oilfield, central Iraq). *Journal of Petroleum Science and Engineering, 209*, 109835.

[2] Aboubacar, M. S. I., Zhang, H., Ousmane, B. I., Li, J., & Cai, Z. (n.d.). An integrated approach for improved permeability and reservoir quality prediction in multiporosity systems, Tahe Ordovician naturally fractured vuggy carbonates.

[3] Al-Mudhafar, W. J., Hasan, A. A., Abbas, M. A., & Wood, D. A. (2025). Machine learning with hyperparameter optimization applied in facies-supported permeability modeling in carbonate oil reservoirs. *Scientific Reports, 15*(1), 12939.

[4] Bao, L.-L., Zhang, J.-S., Zhang, C.-X., Guo, R., Wei, X.-L., & Jiang, Z.-L. (2023). A reliable Bayesian neural network for the prediction of reservoir thickness with quantified uncertainty. *Computers & Geosciences, 178*, 105409.

[5] Chen, J., Zhang, X., Chen, Z., Pang, X., Yang, H., Zhao, Z., Pang, B., & Ma, K. (2021). Hydrocarbon expulsion evaluation based on pyrolysis Rock-Eval data: Implications for Ordovician carbonates exploration in the Tabei Uplift, Tarim. *Journal of Petroleum Science and Engineering, 196*, 107614.

[6] Dawson, H. L., Dubrule, O., & John, C. M. (2023). Impact of dataset size and convolutional neural network architecture on transfer learning for carbonate rock classification. *Computers & Geosciences, 171*, 105284.

[7] De Medeiros, R. S. P., Basso, M., Chinelatto, G. F., Theodoro Soares, M. V., Matheus, G. F., Villacreses Morales, J. F., De Carvalho Mendes, L., & Vidal, A. C. (2024). Unravelling the origin of reworked

deposits in Aptian lacustrine carbonate reservoirs of the Santos Basin, SE Brazil. *Marine and Petroleum Geology, 161*, 106700.

[8] Ding, L., Chen, B., Zhu, Y., Dong, H., & Zhang, P. (2024). Mineral prediction based on prototype learning. *Computers & Geosciences, 184*, 105540.

[9] Gomes, J. P., Bunevich, R. B., Tedeschi, L. R., Tucker, M. E., & Whitaker, F. F. (2020). Facies classification and patterns of lacustrine carbonate deposition of the Barra Velha Formation, Santos Basin, Brazilian Pre-salt. *Marine and Petroleum Geology, 113*, 104176.

[10] Mohammadi, M., Niri, M. E., Bahroudi, A., Soleymanzadeh, A., & Kord, S. (2025). Enhancing formation resistivity factor estimation in carbonate reservoirs using electrical zone indicator and multi-resolution graph-based clustering methods. *Scientific Reports, 15*(1), 30823.

[11] Mohammadian, E., Kheirollahi, M., Liu, B., Ostadhassan, M., & Sabet, M. (2022). A case study of petrophysical rock typing and permeability prediction using machine learning in a heterogenous carbonate reservoir in Iran. *Scientific Reports, 12*(1), 4505.

[12] Montano, D., Gasparrini, M., Gerdes, A., Della Porta, G., & Albert, R. (2021). In-situ U-Pb dating of Ries Crater lacustrine carbonates (Miocene, South-West Germany): Implications for continental carbonate chronostratigraphy. *Earth and Planetary Science Letters, 568*, 117011.

[13] Nawal, M., Kumar, S., & Shekar, B. (2022). LithoBot: An AutoML approach to identify lithofacies. *Second International Meeting for Applied Geoscience & Energy*, 1885-1889.

[14] Qi, L., & Carr, T. R. (2006). Neural network prediction of carbonate lithofacies from well logs, Big Bow and Sand Arroyo Creek fields, Southwest Kansas. *Computers & Geosciences, 32*(7), 947-964.

[15] Silva Dos Santos, V., Gloaguen, E., & Tirdad, S. (2025). Lithological mapping using Spatially Constrained Bayesian Network (SCB-Net): A deep learning model for generating field-data-constrained predictions with uncertainty evaluation using remote sensing data. *Computers & Geosciences, 204*, 105964.

[16] Xin, C., et al. (2023). Integrated carbonate reservoir types modeling based on the PRT deep learning and multi-parameters seismic inversion and its application. *Third International Meeting for Applied Geoscience & Energy Expanded Abstracts*, 1239-1243.

[17] Yang, Y.-Q., Qiu, L.-W., Gregg, J., Shi, Z., & Yu, K.-H. (2016). Formation of fine crystalline dolomites in lacustrine carbonates of the Eocene Sikou Depression, Bohai Bay Basin, East China. *Petroleum Science, 13*(4), 642-656.

[18] Zheng, L., Wang, C., Jiang, Z., Wu, Y., Kong, X., Zhu, X., & Zhang, Y. (2024). Classification and reservoir characteristics of lacustrine carbonate conglomerate in the Shulu Sag of the Bohai Bay Basin. *Marine and Petroleum Geology, 164*, 106806..

Copyright: This work is licensed under a Creative Commons Attribution 4.0 International License, which permits unrestricted use, distribution, and reproduction in any medium, provided the original work is properly cited.

Disclaimer/Publisher's Note: The statements, opinions and data contained in all publications are solely those of the individual author(s) and contributor(s) and not of MOSP and/or the editor(s). MOSP and/or the editor(s) disclaim responsibility for any injury to people or property resulting from any ideas, methods, instructions or products referred to in the content.